Airborne laser scanning proxies of canopy light transmission in forests

Adam Erickson[1,†*], Nicholas Coops[1]

[1]Integrated Remote Sensing Studio, Department of Forest Resources Management, University of British Columbia, 2045-2424 Main Mall, Vancouver, British Columbia, V6T 1Z4, Canada

[†]*Current address*: Hydrological Sciences Laboratory, Code 617, NASA Goddard Space Flight Center, 8800 Greenbelt Rd., Greenbelt, Maryland, 20771, USA

[*]Corresponding author: adam.michael.erickson@gmail.com

ORCID: 0000-0002-8730-073X

Twitter: @admercs

Non-peer-reviewed pre-print submitted to EarthArXiv

Keywords: canopy light transmission; LiDAR; airborne laser scanning; boreal forests; point cloud metrics; area-based metrics

Abstract

Reliable estimates of canopy light transmission are critical to understanding the structure and function of vegetation communities but are difficult and costly to attain by traditional field inventory methods. Airborne laser scanning (ALS) data uniquely provide multi-angular vertically resolved representation of canopy geometry across large geographic areas. While previous studies have proposed ALS indices of canopy light transmission, new algorithms based on theoretical advancements may improve existing models. Herein, we propose two new models of canopy light transmission (i.e., gap fraction, or P_o, the inverse of angular canopy closure). We demonstrate the models against a suite of existing models and ancillary metrics, validated against convex spherical densiometer measurements for 950 field plots in the foothills of Alberta, Canada. We also tested the effects of synthetic hemispherical lens models on the performance of the proposed hemispherical Voronoi gap fraction (P_{hv}) index. While vertical canopy cover metrics showed the best overall fit to field measurements, one new metric, point-density-normalized gap fraction (P_{pdn}), outperformed all other gap fraction metrics by two-fold. We provide suggestions for further algorithm enhancements based on validation data improvements. We argue that traditional field measurements are no longer appropriate for 'ground-truthing' modern LiDAR or SfM point cloud models, as the latter provide orders of magnitude greater sampling and coverage. We discuss the implications of this finding for LiDAR applications in forestry.

Introduction

The light environment is a critical factor for the structure and function of vegetation communities (Dengel and Grace, 2010; Gamon, 2014; Gamon and Bond, 2013; Monsi and Saeki, 2005, 1953). In northern forests, tree crown geometries are well suited to a low solar elevation, occluding less light from neighboring trees (Aakala et al., 2016). Understory light is an important factor in the successional trajectory of forests through vegetation establishment and growth, making it a critical parameter required to forecast forest ecosystems (Canham et al., 1999). Although understory light is a function of quantifiable variation in local stand geometry, topographic position, atmospheric conditions, and solar position, it remains difficult and costly to measure. While the importance of understory light has long been understood (Monsi and Saeki, 1953), it is notoriously difficult to measure with remote sensing methods. The advent of multi-angular remote sensing technologies such as airborne laser scanning LiDAR (ALS) and photogrammetric computer vision have made it possible to map canopy light transmission as a proxy for understory light by assuming beam canopy penetration equivalent to a Poisson process. Monsi & Saeki (1953) were the first to represent contact frequency as a Poisson process, equivalent to the Beer-Lambert law (Hancock, 2010).

Due to limitations in spaceborne sensor resolution and coverage, given the large footprint, fixed satellite track, and single laser path of quantum (i.e., photon-counting) LiDAR sensors such as IceSat GLAS, understory light transmission is difficult to reliably estimate across large areas. While improved sampling is provided by the more recent NASA IceSat-2 ATLAS and Global Ecosystem Dynamics Investigation (GEDI) beam-splitting quantum LiDAR instruments, the improvements will not fully resolve design limitations related to a large (~25m) footprint and limited coverage (Coyle et al., 2015; Dubayah et al., 2014). Data assimilation or imputation techniques are required to generate wall-to-wall maps from sparse spaceborne LiDAR data, increasing the uncertainty of estimates through the inclusion of an additional model. Despite recent advances in deriving forest canopy geometry from commercial passive optical spaceborne sensors (Shean et al., 2016), active optical airborne LiDAR systems remain ideal instruments for estimating understory light conditions at the landscape scale. This is due to the high precision (i.e., point density and geolocation error), broad spatial coverage, and availability of data in many countries, allowing direct measurement of canopy light transmission with multi-angular pulses of near-infrared photons and multi-return or waveform detectors (i.e., photodiodes).

Airborne laser scanning (ALS) is used throughout boreal forests and contains detailed information on forest geometry at scales ranging from stands to landscapes (Wulder et al., 2012). Recent studies have demonstrated a number of ALS metrics of forest structure over large areas, from area-based to individual tree-based approaches (Coops et al., 2007; Hilker et al., 2012; Kaartinen et al., 2012; Lefsky et al., 2002; Popescu et al., 2004, 2002; Varhola et al., 2012; Wulder et al., 2012; Zimble et al., 2003). Studies have also leveraged the increased availability of ALS to estimate understory light regimes in northern forests. Using single-point quantum sensors of photosynthetic photon flux density (PPFD) (Barnes et al., 1993), convex spherical densiometers (Lemon, 1956), or hemispherical photography for ground-level validation, these studies have retrieved a number of relevant canopy light transmission indices (i.e., models, proxies, indicators, metrics, features, or coefficients) from ALS data, including canopy transmittance, canopy gap fraction (P_o), vertical canopy cover (VCC), angular canopy closure

(ACC), effective leaf area index (L_e), apparent clumping index (Ω_{app}), stem density, and basal area (Alexander et al., 2013; Eysn et al., 2015; Kaartinen et al., 2012; Korhonen and Morsdorf, 2014; Moeser et al., 2015; Morsdorf et al., 2006; Musselman et al., 2013; Parent and Volin, 2014; Parker et al., 2001; Popescu et al., 2002; Richardson et al., 2009). Such indices are desirable for their simplicity and physical geometric basis, aiding interpretation efforts, as well as their ability to be ingested as engineered features into machine learning models in large-area mapping (Domingos, 2012).

Many of these ALS metrics may be readily applied as indices of canopy light transmission, individually or in combination. Some of the earliest, simplest, and most effective metrics of ACC and thus P_o are based on the ratio of ground-to-canopy returns (Korhonen et al., 2011; Morsdorf et al., 2006; Riaño et al., 2004; Solberg et al., 2009). The metric of Solberg *et al.* (2009) differs in that it corrects for pulses that have returns from both the canopy and ground, assigning a partial cover value to these. A pulse intensity-based approach was designed to correct for two-way transmission loss (Hopkinson and Chasmer, 2007), also novel for utilizing target reflectance information. More recent approaches provide hemispherically projected LiDAR metrics comparable to traditional ground measurements (Parent and Volin, 2014; Varhola et al., 2012), while others further utilize geometric operations to improve the estimation of cover (Alexander et al., 2013). An opportunity exists to improve simple transmission metrics and advanced representations of forest geometry to estimate cover, as the theory surrounding both continue to improve. While future studies should apply deep neural networks designed for scattered, unordered point data, such as using models based on the PointNet++ architecture (Qi et al., 2017), we focus on simple geometric operations for their diminished need for labeled data and speed/ease of computation in large-area mapping applications.

Calculations of forest structural parameters from ALS are often distinct from those of traditional ground methods, due to differences in sampling bias (top- vs. bottom-of-canopy), lending to variation in terminology and methodology. Canopy light attenuation calculations based on ALS often assume canopy light transmission (T) equivalent to canopy gap fraction (P_o), each inverses of vertical canopy cover (VCC) and angular canopy closure (ACC), as provided in the following equation (Gonsamo et al., 2013; Hopkinson and Chasmer, 2009; Morsdorf et al., 2006):

$$T = P_o = 1\text{-ACC} = 1\text{-VCC}$$

Traditionally, VCC quantifies the 2-D areal canopy coverage, while T is a function of incident photosynthetically active radiation (PAR), fraction of absorbed PAR (fPAR) by leaf absorptance, leaf transmissivity, and scattering, incorporating leaf chemistry, geometry, position, and orientation effects on the bidirectional reflectance distribution function, or BRDF (Gastellu-Etchegorry et al., 1996). While the equivalence of T and P_o holds in the absence of detailed information, the two metrics remain distinct, providing different – though complementary – information (Gonsamo et al., 2013).

Although ALS pulses are typically emitted at narrow zenith angles less than 20 degrees from nadir, they provide an empirical test of angular light penetration through the canopy, making ALS suitable for estimating P_o. Meanwhile, VCC is often calculated from ALS for each cell using narrow incoming zenith angles between 0 and 10, opposite to scan and beam divergence source angle (Morsdorf et al., 2006; Weiss et al., 2004). Hence, the measurement of VCC with ALS is often a field-of-view, or scope, function (Lee et al., 2008), rather than a true measure of 2-D areal coverage (although simple grid-based methods exist), making it sensitive to neighborhood effects. Here, as with leaf area index (L), gridded ALS-derived metrics (e.g., the ratio of canopy first-returns to ground first-returns) are more compatible with the classical definition of VCC. Similar challenges of sampling bias have been reported for gap fraction (P_o) estimates derived from terrestrial laser scanning (TLS) LiDAR (Vaccari et al., 2013).

The objective of this study was to develop new ALS metrics and regression models of T that can be extended to forest landscape models to simulate understory irradiation across large areas. Four new ALS metrics for retrieving T are presented, including hemispherical Voronoi gap fraction (P_{hv}), point-density normalized gap fraction (P_{pdn}), and their inverses, hemispherical Voronoi angular canopy closure (ACC_{hv}) and point-density normalized angular canopy closure (ACC_{pdn}). While P_{hv} and ACC_{hv} are intended to improve estimates of canopy light interception from LiDAR with varying sensor properties, P_{pdn} and ACC_{pdn} are intended to reduce sensor effects by normalizing hemispherical sectors by their surface area and the overall point density.

The four new hemispherical canopy metrics (P_{hv}, P_{pdn}, ACC_{hv}, and ACC_{pdn}), nine vertical canopy cover (VCC) metrics, twelve stem and crown metrics, and five other metrics, for a total of 30 metrics (Table 1), were validated against traditional coarse-resolution convex spherical densiometer ground measurements of angular canopy closure (ACC), representing the inverse of T. The P_{hv} metric was applied using four different hemispherical lens geometries at canopy height thresholds varying from one meter to five meters in 0.25 m steps, for a total of 68 different P_{hv} configurations for each plot. In doing so, we provide key innovations that are readily deployable across a range of forested systems with available ALS data, as the P_{pdn} method is designed to overcome common shortcomings related to changes in LiDAR sensor design over time. Thus, it is anticipated that the P_{pdn} method may be highly valued by the forestry industry for operational use. Furthermore, we provide a future direction for research along both detailed geometric and generalized coefficient approaches. Finally, we make all of our innovations openly available for use in the *gapfraction* package for R (https://adamerickson.xyz/gapfraction/).

Table 1. Understory light metrics calculated in this study, explained in detail in the following section

New Metrics	Vertical Canopy Cover Metrics	Tree and Crown Metrics	Other Metrics
Hemispherical Voronoi gap fraction (P_{hv})	Above-height cover index (VCC_{aci})	Moving window n trees (ITC_{mw})	Beer-Lambert Law gap fraction (P_{bl})
Point-density normalized gap fraction (P_{pdn})	Beer's Law-modified-intensity-return ratio (VCC_{bl})	Moving window crown area (G_{mw})	Beer-Lambert Law effective leaf area index (Le_{bl})
Hemispherical Voronoi angular canopy closure (ACC_{hv})	Cartesian Voronoi fractional cover (VCC_{cv})	Hierarchical moving window n trees (ITC_{hmw})	Ground-to-total-return ratio effective leaf area index (Le_{r})
Point-density normalized angular canopy closure (ACC_{pdn})	First-echo cover index (VCC_{fci})	Hierarchical moving window crown area (G_{hmw})	Contact frequency effective leaf area index (Le_{n})
	Canopy-to-total-first-return ratio (VCC_{fr})	Watershed n trees (ITC_{wat})	Apparent clumping index (Ωapp or ACI)
	Intensity-return ratio (VCC_{ir})	Watershed crown area (G_{wat})	
	Canopy-to-total-pixel ratio (VCC_{p})	Hierarchical watershed n trees (ITC_{hwat})	
	Canopy-to-total-return ratio (VCC_{r})	Hierarchical watershed crown area (G_{hwat})	
	Solberg's cover index (VCC_{sci})	Distance and direction to canopy (C_{dist}, C_{dir})	
		Distance and direction to tree crown (Cr_{dist}, Cr_{dir})	

Materials and methods

Vegetation ground plot measurements were collected in the Hinton Forest Management Area in the early 2000s during summer (leaf-on) conditions. While details of the area have been documented in previous research (Nielsen, 2005; Nielsen et al., 2006, 2004), the foothills region is generally characterized by monospecific stands of lodgepole pine (*Pinus contorta* Douglas ex Louden), well-drained post-glacial soils, moderate temperatures and precipitation, and extensive forest management (Natural Regions Committee, 2006). Angular canopy closure (ACC), and thus canopy gap fraction (P_o = 1-ACC), was measured from breast-height using a convex spherical densiometer. Densiometer measurements were recorded for each of the four cardinal directions and averaged for each plot (Lemon, 1956; Nielsen, 2005).

ALS data were provided by Foothills Research Institute on behalf of Hinton Wood Products, a subsidiary of West Fraser. The sorties were conducted by a Canadian remote sensing company, Airborne Imaging, in the mid-2000s near Hinton, Alberta in the foothills of the Canadian Rocky Mountains. Airborne Imaging used an Optech Airborne Laser Terrain Mapper (ALTM) 3100 mounted aboard a twin-engine fixed-wing Piper Navajo aircraft with an Applanix precision global positioning system-inertial navigation system (GPS-INS) position-orientation system utilizing sensor fusion. Flights were conducted with 50% sidelap between flight lines at an estimated mean velocity of ~ 160 knots (296 km h^{-1}) and altitude of ~ 1,400 m above-ground-level (AGL), yielding an estimated mean point spacing of 0.75 m and theoretical minimum vertical accuracy between 10 and 15 centimeters (±1 sigma). The Optech ALTM 3100 emitted near-infrared (1,064 nm) photons at a pulse rate of 70 kHz, using a maximum scan angle from nadir of ~ 14 degrees (0.24 radians), scan rate of 33 Hz, and a sawtooth scanning pattern. While the Optech ALTM 3100 is one of the first commercial ALS systems capable of full-waveform digitization, the system used in this study is a discrete-return system, recording up to four returns for every laser pulse, each with 12-bit dynamic range intensity information (Hilker et al., 2013).

Ground and non-ground returns were classified using Terrasolid TerraScan version 0.6 consumer-off-the-shelf (COTS) software, which applies previously demonstrated methods (Kraus and Pfeifer, 1998). The pre-processed LiDAR data were delivered in standard American Society of Photogrammetry and Remote Sensing (ASPRS) laser (LAS) file specification. The estimated final horizontal and vertical positional accuracy was 0.45 m and 0.3 m, respectively, based on a large sortie conducted on November 19, 2007 (Hilker et al., 2013). A total of 18.6 billion points were collected at a mean point density of 1.64 points m^{-2} for the 1,100 km^2 Hinton area, based on calculations with LAStools software (Isenburg, 2015).

For model development, 100 field plots representing different levels of forest cover containing both densiometer measurements and complete ALS coverage were randomly sampled. Each plot contained one value for ACC, measured at the plot center. This sampling strategy allowed us to capture a wide distribution of ACC values. Following model development, the top performing metric was validated for all 950 field plots.

Data pre-processing

Using LAStools (Isenburg, 2015), the ALS tiles were height-normalized before extracting circular field plots with a 50 m radius, based on previous research exhibiting a saturation of edge effects below this radius threshold (Alexander et al., 2013; Zhao and Popescu, 2009). Normalization consisted of extracting the ground plane from the point data and subtracting the

Delaunay triangle-position elevation from each return's *z* value. LAStools implements an optimized variant of the best available ground plane extraction algorithm (Axelsson, 1999; Maguya et al., 2014), modified to include Delaunay streaming or triangulated irregular network (TIN) streaming (Isenburg et al., 2006b, 2006a, 2006c) for improved computational efficiency on large datasets. Maximum point height was filtered at 40 m, based on local tree species ground measurements. The ALS plots were processed with a series of point cloud metrics implemented in custom R scripts (R Core Team, 2015), described below. Finally, the top performing ALS metric (VCC_{fci}) was applied to an expanded set of ALS plots to analyze variation related to species composition and age class.

Spike-free canopy height model algorithm

The first step required the generation of continuous canopy height models (CHMs) without smoothing- or sampling-related artifacts. This was due to pitting in the simple gridded maxima CHMs given a mean point density below 2 points m^{-2}, known to affect the accuracy of tree detection. In order to improve CHM inputs for individual tree crown (ITC) detection, a layered 2-D adaptation of the spike-free CHM algorithm (Khosravipour et al., 2016, 2014) was implemented. The approach uses vertically stratified 2-D Delaunay triangulation with barycentric interpolation along *z*-values for triangulated irregular network (TIN) generation. The maximum of the resulting vertical surface model layers or slices is then computed, yielding a CHM with reduced spiking.

Equivalent in output to the original, our modified implementation of the spike-free CHM algorithm vertically stratifies all returns into user-defined windows or slices to constrain

Delaunay triangulations, which can be absolute distances or height percentiles. A 2 m height threshold was used with steps at 5, 10, and 15 m, as in the pit-free CHM work (Khosravipour et al., 2014). Delaunay triangles with edge lengths exceeding a user-defined threshold are filtered to limit smoothing, set to the default value (Khosravipour et al., 2014). The final CHM consists of continuous height maxima along raster grid points. This adaptation takes advantage of vertical stratification to generate non-overlapping points necessary for 2-D Delaunay triangulation. The theoretical advantage over the 3-D Constrained Delaunay approach (Khosravipour et al., 2016) is chiefly computational for the sake of speed and simplicity. These and other functions are provided in the *gapfraction* package for R (https://adamerickson.xyz/gapfraction/).

Hemispherical Voronoi gap fraction

The hemispherical Voronoi gap fraction (P_{hv}) index represents P_o as the areal coverage of Voronoi tessellation cells above a given canopy height threshold from the perspective of standing at the plot center and looking toward the zenith, identical to a traditional hemispherical photograph. The plot center at 3-D local Cartesian coordinate $(x=0, y=0, z=0)$ is set equal to the hemispherical camera model principal point, or intersection of the optical axis and image plane. The ground plane is set equal to the image plane, with the optical axis pointing skyward at the zenith. Once the LiDAR data is pre-processed into normalized heights and local Cartesian coordinates, the first step is to re-project the LiDAR points into image coordinates based on a model of a fisheye (hemispherical) lens.

The projection of a 3-D point $\boldsymbol{X}_w = (\boldsymbol{X}_w, \boldsymbol{Y}_w, \boldsymbol{Z}_w)^T$ into a 2-D image sensor coordinate $\boldsymbol{x}'_j = (\boldsymbol{x}'_j, \boldsymbol{y}'_j)$ requires a mathematical model of a fisheye lens, consisting of a series of transformations with extrinsic and intrinsic camera parameters (Abraham and Förstner, 2005; Ray, 2002). The extrinsic parameters map the real-world coordinates into camera coordinates, while the intrinsic parameters map the camera coordinates onto the image plane. The image coordinate calculations take the following form (Abraham and Förstner, 2005):

$$x' = c_x \cos(\varphi)\, r^*(\theta) + x'_H$$

$$y' = c_y \sin(\varphi)\, r^*(\theta) + y'_H$$

Here, c_x and c_y are the principal distances (this allows for non-square pixels), φ and θ are the azimuthal and polar angles, respectively, $r^*(\theta)$ is the radial projection function, or mapping function, and, x'_H and y'_H are the coordinates of the principal point, or the intersection of the optical axis and the image plane. The distortion model parameters used for real-world lenses, $\Delta x'$ and $\Delta y'$, typically added to the end of their corresponding equations, are omitted. To change to a different hemispherical camera model, the radial projection function can be simply modified.

The classical pinhole camera is described by the *perspective* projection function of the form $r' = c \tan(\theta)$, where r' is the radial distance from the principal point on the image plane and c is the principal distance, a function of the focal length and focal distance (Fourcade, 1928). Fisheye lenses generally use one of four common radial projection functions: *stereographic*, *equidistant*, *orthogonal*, and *equisolid angle*. Most consumer fisheye lenses use the *equisolid angle* projection and have a full-frame design (the picture angle is 180° only when measured diagonally and is smaller elsewhere), while scientific lenses utilized for hemispherical photography typically use the *equidistant* projection, where the radial distance is equal to the polar angle, and have a circular design (the full 180° hemisphere is recorded within the image plane). Here, all four projections are implemented with a circular design in the *gapfraction* package for R. The radial projection function, or mapping function, for each projection is as follows (Abraham and Förstner, 2005; Ray, 2002):

$r' = c \tan(\theta/2)$	Stereographic projection
$r' = c\, \theta$	Equidistant projection
$r' = c \sin(\theta)$	Orthogonal projection
$r' = c \sin(\theta/2)$	Equisolid angle projection

To transform the real-world coordinates to camera coordinates, the normalized point clouds were projected into 3-D local Cartesian coordinates with an *(x, y, z)* tuple centroid of *(0, 0, 0)*. A function was developed that allows this calculation without plot center geolocation information to ease LiDAR plot processing. The function sets the midpoint of the vector of *X* and *Y* values to half of the range, as shown below:

$$x' = x - x_{min} - \left(\frac{x_{max} - x_{min}}{2}\right)$$

$$y' = y - y_{min} - \left(\frac{y_{max} - y_{min}}{2}\right)$$

To transform the camera coordinates into image plane coordinates, the 3-D local Cartesian coordinates are projected into 2-D polar coordinates (azimuth angle and radial distance, or φ and r) before projecting the 2-D polar coordinates into 2-D Cartesian space with standard trigonometric equations, where $x' = r \cos(\varphi)$ and $y' = r \sin(\varphi)$. The calculations were implemented in their normalized image plane form (Abraham and Förstner, 2005), as the 3-D local Cartesian coordinates were normalized to their true distance values in meters, rather than the typical unit sphere. This was done to preserve 3-D Cartesian distances for calculations that do not require hemispherical or image plane projections.

Once the LiDAR data were projected onto the 2-D hemispherical image plane, the 2-D Delaunay triangulation and Voronoi tessellation were computed for the planar point sets using the *deldir* package for R (Turner, 2015), filtering points below a user-defined canopy threshold. The summed area of filtered cells, or gaps, was calculated as a percentage of the overall plot area, providing the hemispherical Voronoi gap fraction (P_{hv}). This assumes 100% light occlusion by non-filtered cells. The implication of this simplification is that light attenuation is overestimated, which can be adjusted by a simple transmissivity coefficient derived from the slope of linear regression. Since this work focuses on correlations and regression model development, calculating such a coefficient was not necessary. To calculate ACC_{hv}, P_o values were subtracted from 1. Last, a height-threshold sensitivity analysis was conducted by applying the function with each of the four fisheye lens models and each of 17 minimum canopy height thresholds ranging from 1 to 5 m, at a step of 0.25 m, producing 68 unique combinations for each of the 100 plots, for a total of 6,800 iterations.

Point-density normalized gap fraction

The point-density normalized gap fraction (P_{pdn}) is based on partitioning hemispherically projected first-return points into polar and azimuthal sectors, or annuli, then calculating the number of points per sector as a proxy for canopy light occlusion. Removing non-first-returns facilitates the calculation of point-density normalized metrics by evening the point spacing along the Cartesian ground plane, with ground returns representing canopy gaps. Otherwise, the spatial bias of sampling is too high for the normalization procedure. The return values were normalized by the ground point density and the surface area of each hemisphere sector to reduce sensor effects, producing similar P_{pdn} values for vastly different point densities. This follows the logic that a greater number of points are expected for sections of greater surface area, given evenly spaced sampling and thus a relatively constant point density along the (X, Y) plane. The procedure begins by filtering for first-returns and projecting the 3-D Cartesian coordinates (X, Y, Z) into spherical coordinates (r, φ, θ) using standard equations:

$$r = \sqrt{x^2 + y^2 + z^2}$$

$$\varphi = \cos^{-1}\left(\frac{z}{r}\right)$$

$$\theta = \tan^{-1}\left(\frac{y}{x}\right)$$

The φ values were rescaled from $(-\pi, \pi)$ to the interval $(0, 2\pi)$ by adding 2π to φ values where φ is less than zero. Based on previous research (Zhao & Popescu, 2009), the spherical coordinates were sectioned at polar and azimuthal increments of 5° and 45°, respectively, producing 18 x 8 sky sectors for a total of 144 sectors. A polar resolution of 15° is also commonly used in LiDAR studies (Korhonen and Morsdorf, 2014), but is likely coarser than necessary for modern sensors. The number of first returns per hemispherical sector was calculated using the following equation:

$$\theta_{returns_i} = \{P \vee \theta_i < \theta_P < \theta_{i+1}\}$$

$$\varphi_{returns_j} = \{P \vee \varphi_j < \varphi_P < \varphi_{j+1}\}$$

$$C(returns_{i,j}) = P \vee P \in \{\theta_{returns_i} \cap \varphi_{returns_j}\}$$

Here, $C(returns_{i,j})$ is the number of elements contained in a set defined by the intersection of polar and azimuthal angle subsets, $\theta_{returns_i}$ and$\varphi_{returns_j}$, at hemisphere sector intervals defined by steps *i* and *j*, respectively. A matrix is produced containing the frequency of returns within each sector of the hemisphere. In order to account for varying sector sizes, the values are adjusted by the hemispherical surface area of each sector. To do so, the surface area of each hemispherical sector is first calculated, as follows:

$$A_{i,j} = R^2$$

This produces a second matrix of equal dimensions, *i x j*. Here, $A_{i,j}$ is the area of a sector for polar angle Θ_i and azimuth angle φ_j at intervals defined by steps *i* and *j*, while *R* is the radius of the sphere. Next, matrix division is performed on the return frequency and surface area matrices, normalized by point density for the full hemisphere along the *(X, Y)* Cartesian plane. This mitigates issues related to sensor effects (e.g., point density). The filtering of non-first-returns is necessary to also reduce sensor effects along the *z*-axis, as vertical resolution can vary due to a number of factors. Point-density normalized canopy gap fraction (P_{pdn}) was calculated with the following equation:

$$P_{pdn}=\sum_{i=1}^{n}\sum_{j=1}^{n}\left(\frac{\frac{n_{First\ Returns_{i,j}}}{D_{FirstReturns}}}{A_{Sector_{i,j}}}x\,\frac{A_{Sector_{i,j}}}{A_{Hemisphere}}\right)$$

Where $n_{First\ Returns_{i,j}}$ is the count of first returns in matrix **C** for hemisphere sector **C**[*i*-*j*], $A_{Sector_{i,j}}$ is the surface area in matrix **A** of sector **A**[*i*, *j*], $D_{FirstReturns}$ is the point density for the full dataset along the Cartesian *(X, Y)* ground plane, and $A_{Hemisphere}$ is the surface area of the full hemisphere. The right-hand side of the summation scales the output by the proportion of the hemisphere occupied by each sector, similar to the scaling of L_e by polar angle (Korhonen and Morsdorf, 2014), rather than calculating the mean value without accounting for sector size. In essence, the P_{pdn} function normalizes the number of returns per sector by the overall point density and the sector surface area, with the output values scaled by hemisphere proportion. Double summation is approximate to a double integral. ACC_{pdn} is merely one minus P_{pdn}, as its inverse.

Comparison with other ALS metrics

A set of standard metrics were also implemented to assess their performance against new methods and ground measurements. The method comparison framework includes estimates of canopy gap fraction, angular canopy closure, vertical canopy cover, individual tree detection, crown area, distance to crown and canopy, leaf area index, and clumping. First, these methods are described in the following paragraphs.

Based on previous research on the estimation of leaf area index (Lang and Yueqin, 1986; Miller, 1967; Ryu et al., 2010; Zhao and Popescu, 2009), the effective leaf area index (L_e) was calculated using the following equation (Korhonen and Morsdorf, 2014):

$$L_e = 2\sum_{i=1}^{n} -\ln \overline{P(\theta_i)} \cos\theta \frac{\sin\theta_i}{\sum_{j=1}^{n} \sin\theta_j}$$

The apparent clumping index (Ω_{app}) was calculated based on a ratio of two L_e estimation methods (Ryu et al., 2010). The previous approach was modified by approximating the integral as a summation, with each L_e method weighted by the *sine* of the given polar angle, θ (Korhonen and Morsdorf, 2014):

$$\Omega_{app} = \frac{2\sum_{i=1}^{n} -\ln \overline{P(\theta_i)} \cos\theta \frac{\sin\theta_i}{\sum_{j=1}^{n} \sin\theta_j}}{2\sum_{i=1}^{n} -\overline{\ln P(\theta_i)} \cos\theta \frac{\sin\theta_i}{\sum_{j=1}^{n} \sin\theta_j}}$$

Next, the L_e vector is used for n polar angles θ to calculate the canopy gap fraction per the Beer-Lambert Law (Monsi and Saeki, 2005, 1953):

$$P_{o_i} = \exp\left(\frac{-L_e G(\theta_i)}{\cos\theta_i}\right)$$

Other metrics include the following vertical canopy cover (VCC) metrics: canopy-to-total-return ratio (VCC_r) (Morsdorf et al., 2006), canopy-to-total-first-return ratio (VCC_{fr}) (Morsdorf et al., 2006), intensity-return ratio (VCC_{ir}) (Hopkinson and Chasmer, 2009), Beer's Law-modified-intensity-return ratio (VCC_{bl}) (Hopkinson and Chasmer, 2009) or intensity cover index (ICI) (Korhonen and Morsdorf, 2014), above-height cover index (VCC_{aci}) (Richardson et al., 2009), first-echo cover index (VCC_{fci}) (Korhonen et al., 2011; Korhonen and Morsdorf, 2014), Solberg's cover index (VCC_{sci}) (Solberg et al., 2009), canopy-to-total-pixel ratio (VCC_p) (Parent and Volin, 2014), and Cartesian Voronoi fractional cover (VCC_{cv}) (Alexander et al., 2013). These metrics were applied with a canopy threshold of 1.25 m, per two seminal studies demonstrating algorithms that are the primary basis of this work (Alexander et al., 2013; Morsdorf et al., 2006).

Table 2. Additional VCC metrics

Metric	Equation
Canopy-to-total-return ratio	$VCC_r = \frac{\sum N_{All>1.25m}}{\sum N_{Last} + N_{Single}}$
Canopy-to-total-first-return ratio	$VCC_{fr} = \frac{\sum N_{All>1.25m}}{\sum N_{First}}$
Intensity-return ratio	$VCC_{ir} = \frac{\sum I_{Ground}}{\sum I_{All}}$
Beer's Law-modified-intensity-return ratio	$VCC_{bl} = \frac{\left(\frac{\sum I_{Ground\ Single}}{\sum I_{All}}\right) + \sqrt{\frac{\sum I_{Ground\ Last}}{\sum I_{All}}}}{\left(\frac{\sum I_{First} + \sum I_{Single}}{\sum I_{All}}\right) + \sqrt{\frac{\sum I_{Intermediate} + \sum I_{Last}}{\sum I_{All}}}}$
Above-height cover index	$VCC_{aci} = \frac{\sum N_{Single} + N_{All>1.25m} + N_{Intermediate} + N_{Last}}{\sum N_{All}}$
First-echo cover index	$VCC_{fci} = \frac{\sum N_{Single>1.25m} + \sum N_{First>1.25m}}{\sum N_{Single} + \sum N_{First}}$
Solberg's cover index	$VCC_{sci} = \frac{\sum N_{Single>1.25m} + 0.5\left(\sum N_{First>1.25m} + \sum N_{Last>1.25m}\right)}{\sum N_{Single} + 0.5\left(\sum N_{First} + \sum N_{Last}\right)}$
Canopy-to-total-pixel ratio	$VCC_p = \frac{\sum N_{CHM>1.25m}}{\sum N_{CHM}}$
Cartesian Voronoi fractional cover	$VCC_{cv} = V\left(P_{First\ Return}\right) > 1.25m$

A suite of proxy metrics relevant to the calculation of P_o was also tested. These include individual tree crown (ITC) counts using maximum and hierarchical variable-moving-window

(ITC_{mw}) (Koch et al., n.d.; Popescu et al., 2002) and watershed (ITC_{wat}) algorithms (Hyyppa et al., 2001; Zhao and Popescu, 2007), crown area (G) using detected tree heights with an empirical height-to-crown-radius function, distances and directions to nearest crown(C_{dist}, C_{dir}) and canopy pixels (Cr_{dist}, Cr_{dir}) from the plot center (Moeser et al., 2015), effective leaf area index (L_e) based on the Beer-Lambert Law (Korhonen and Morsdorf, 2014; Monsi and Saeki, 1953), L_e based on the ground-to-total-return ratio (Richardson et al., 2009), and L_e based on contact frequency (Morsdorf et al., 2006), apparent clumping index (Ω_{app}) (Ryu et al., 2010), and Beer-Lambert Law canopy gap fraction (P_{bl}) (Monsi and Saeki, 2005, 1953; Ryu et al., 2010). While the ITC results may not be physically meaningful in this case, as they were not locally validated, we analyze these values for correlation with T in a classical feature engineering approach. Correlations with convex spherical densiometer measurements were calculated before testing univariate and multivariate linear models with stepwise-AIC and -BIC model selection.

Tree and crown metrics

In order to perform individual tree crown (ITC) detection and crown area estimation, empirical data from recent research in the study area (Cortini et al., 2011) was applied to model the height-to-crown-area relationship for deciduous and conifer species, as well as all species as one group. The ground data consist of aggregated minima, means, and maxima for major regional tree species height-to-crown-area, with standard deviations provided. Models for height-to-crown-area were developed for aggregated native species in the study area from these statistical moments.

Correcting for temporal mismatch

The effect of filtering sites likely disturbed between spherical densiometer and ALS sampling campaigns was tested, in order to correct for a half-decade mismatch in data collection. This filtering process was also used to correct for discontinuity between ground and remote sensing observations due to seasonal changes in leaf area index, as ground observations were generally collected during summer leaf-on conditions while ALS sorties were conducted in fall leaf-off conditions. The error contribution of leaf state is likely minimal, as evergreen forest is dominant in the study area (Nielsen, 2005). Observations with ground-based angular canopy closure (ACC) values below 0.10 were filtered or removed, where disturbances or leaf condition discontinuities were apparent in ground-to-ALS ACC plots. Observations were filtered if the ground ACC value, collected at a later date (i.e., potentially subject to disturbance), was less than 0.1 and showed a reduction of 0.1 or more.

Results

Estimation of ACC and P_o as a proxy for T using ALS data showed good performance. Regression models using multiple metrics substantially outperformed any single ALS metric, yet individual metrics have utility for their simplicity and physical basis, facilitating interpretation. Of the individual metrics, VCC_{fci}, showed the best performance.

ALS Estimates of ACC and P_o

To test for correlations, given the perfectly inverse relationship between gap fraction (P_o) and angular canopy closure (ACC), absolute values were used to calculate Pearson's correlation coefficient (r) against convex spherical densiometer measurements of ACC. The top five results in terms of r were all vertical canopy cover metrics, with the strongest correlation shown for VCC_{fci} (r = 0.61), followed by VCC_{sci} (r = 0.61), VCC_{fr} (r = 0.60), VCC_{r} (r = 0.58), and VCC_{ir} (r = 0.57). The two variable-window individual tree crown (ITC) detection algorithms followed, at r = 0.57 for each, demonstrating their utility as a proxy for T, while point-density normalized P_o (P_{pdn}) was the highest performing new and gap fraction metric at r = 0.56.

Each virtual fisheye lens model in P_{hv} improved in accuracy as the minimum canopy height increased, with the equisolid angle model showing the poorest results (Figure A2.1). An optimal canopy height threshold was indicated of 5 m for all hemispherical lens models tested, indicative of an under-prediction of ACC. Of all the gap fraction metrics, P_{pdn} showed the strongest negative correlation and thus closest agreement with ground ACC measurements. VCC_{fci}, which showed the strongest correlation with ground ACC data, was strongly correlated with the following LiDAR metrics: VCC_{fr} (r = 0.99); VCC_{sci} (r = 0.99); VCC_{r} (r = 0.98); VCC_{ir} (r = 0.97); VCC_{p} (r = 0.97).

ITC detection methods show a strong negative correlation with the Beer-Lambert Law gap fraction (P_{bl}), while the point-density normalized gap fraction (P_{pdn}) shows a strong negative relationship with VCC metrics. Meanwhile, P_o and VCC metrics show strong similarity within metrics. The hierarchical clustering of the hemispherical Voronoi gap fraction (P_{hv}) results indicates that correlations are more strongly linked to minimum canopy height than to the fisheye lens model used. A canopy height threshold of 5 m was indicated for all P_{hv} metrics.

ITC counts similarly have a strong negative correlation with P_{hv} metrics with a higher minimum canopy height, but not with lower height thresholds. Meanwhile, metrics such as Ω_{app}

and direction to canopy or crown have very low correlations with other variables, as expected. The strong negative correlation of P_{pdn} with VCC metrics, and weak correlation with P_{hv} metrics, suggests that the two gap fraction metrics capture fundamentally different properties of forest geometry. Meanwhile, the Beer-Lambert Law gap fraction (P_{bl}) shows strong correlations with empirical ITC crown area estimates.

Removing post-disturbance sites (sites with ground ACC values below 0.1 and ALS values greater by 0.1 or more) before sampling the ground plots, the top seven metrics, in terms of univariate linear model fit with ground measurements, were all vertical canopy cover (VCC) metrics (Figure 1). Of these, the first-echo cover index (VCC_{fci}) (Korhonen et al., 2011; Korhonen and Morsdorf, 2014) again achieved the highest score. The seven top metrics include VCC_{fci} (R^2 = 0.53), VCC_{fr} (R^2 = 0.51), VCC_{ir} (R^2 = 0.51), VCC_{sci} (R^2 = 0.51), VCC_r (R^2 = 0.49), VCC_{cv} (R^2 = 0.48), and VCC_p (R^2 = 0.47). While P_{pdn} performed well before filtering out sites, at ninth best (R^2 = 0.32), it subsequently dropped to eleventh (R^2 = 0.38) after filtering sites. Meanwhile, the ITC count metrics and hierarchical watershed-based crown area performed surprisingly well; these metrics produced R^2 values for ACC approximately double those of the P_{hv} metrics. Meanwhile, ACC R^2 values for P_{pdn} doubled those of other P_o methods, including P_{hv}.

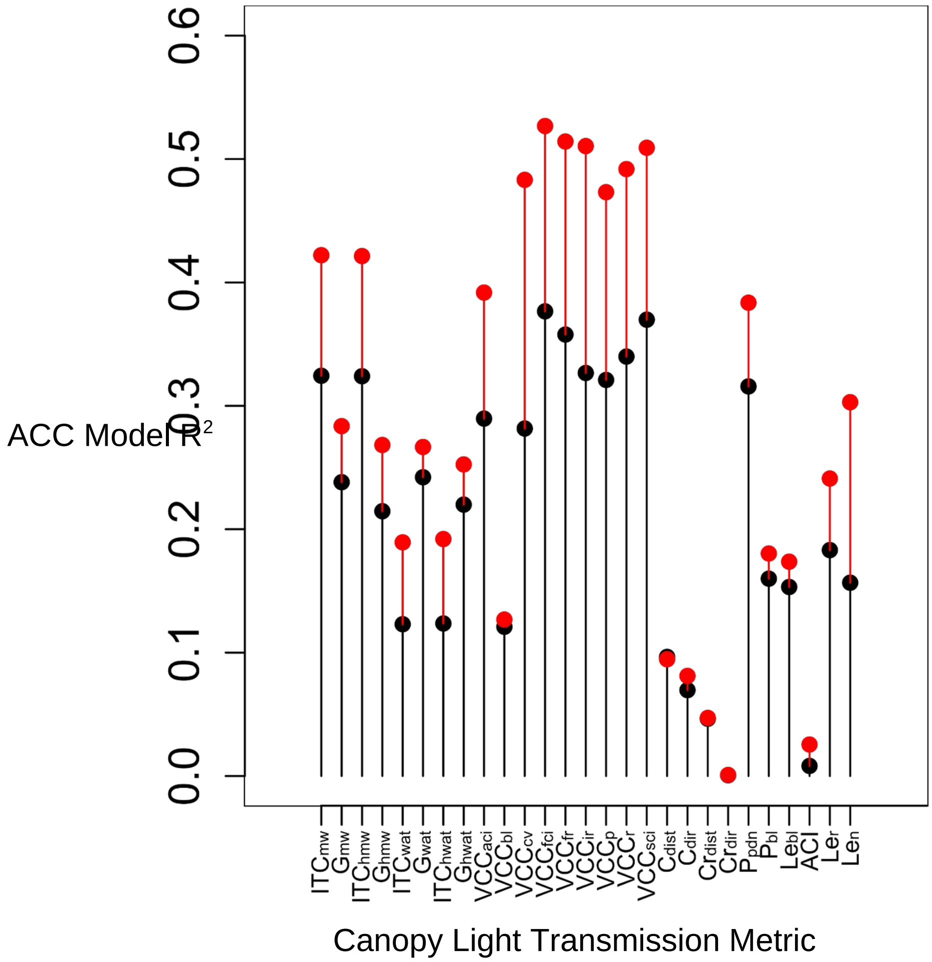

Figure 1. Univariate linear model angular canopy closure (ACC) model R^2 by metric for all sites and without disturbed or temporally non-synchronous sites in terms of LAI seasonality; black = all sites; red = without flagged sites

An equiangular hemispherical lens projection appeared particularly sensitive to the inclusion of sites that were disturbed or temporally inconsistent with ALS sorties, as filtering out these sites substantially improved model performance (Figure 2).

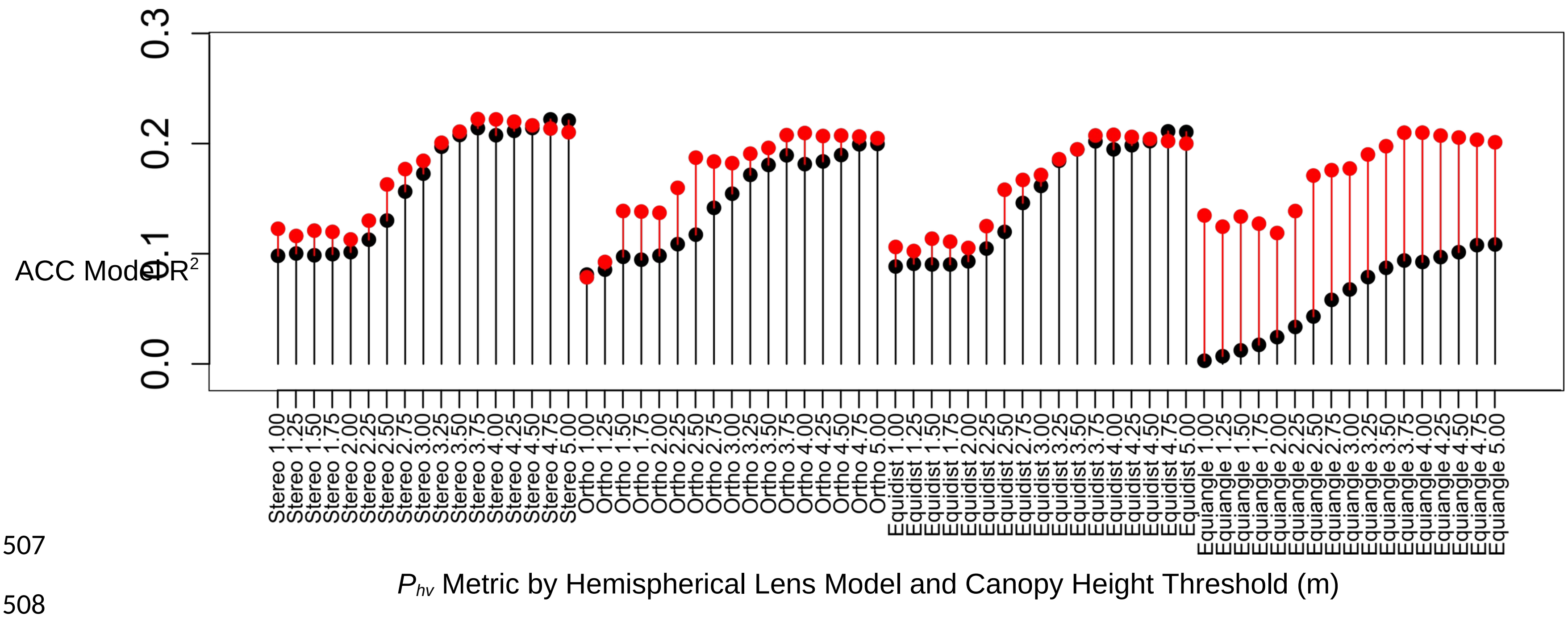

Figure 2. Change to univariate linear model of angular canopy closure (ACC) model R^2 by metric due to filtering likely disturbances; red points represent the filtered values; x-axis labels use the following convention: [*lens model*] [*canopy height threshold*]; Stereo = stereographic projection; Ortho = orthographic projection; Equidist = equidistant projection; Equiangle = equisolid angle projection

The mean R^2 improvement attributable to filtering out disturbances was $\Delta R^2 = +0.05$. The largest gains were shown by VCC_{cv} ($\Delta R^2 = +0.20$), VCC_{ir} ($\Delta R^2 = +0.18$), VCC_{fr} ($\Delta R^2 = +0.16$), VCC_p ($\Delta R^2 = +0.15$), and VCC_r ($\Delta R^2 = +0.15$), while the largest loss was shown by the stereographic and equidistant fisheye lens model P_{hv} metrics at a minimum canopy height of five meters ($\Delta R^2 = -0.01$). Overall, VCC metrics, ITC metrics, and the equisolid angle P_{hv} metrics showed the greatest model improvement, indicating sensitivity to disturbance- or leaf area-related noise. Figure 3 shows the full P_{hv} calculation process conducted for each site tested.

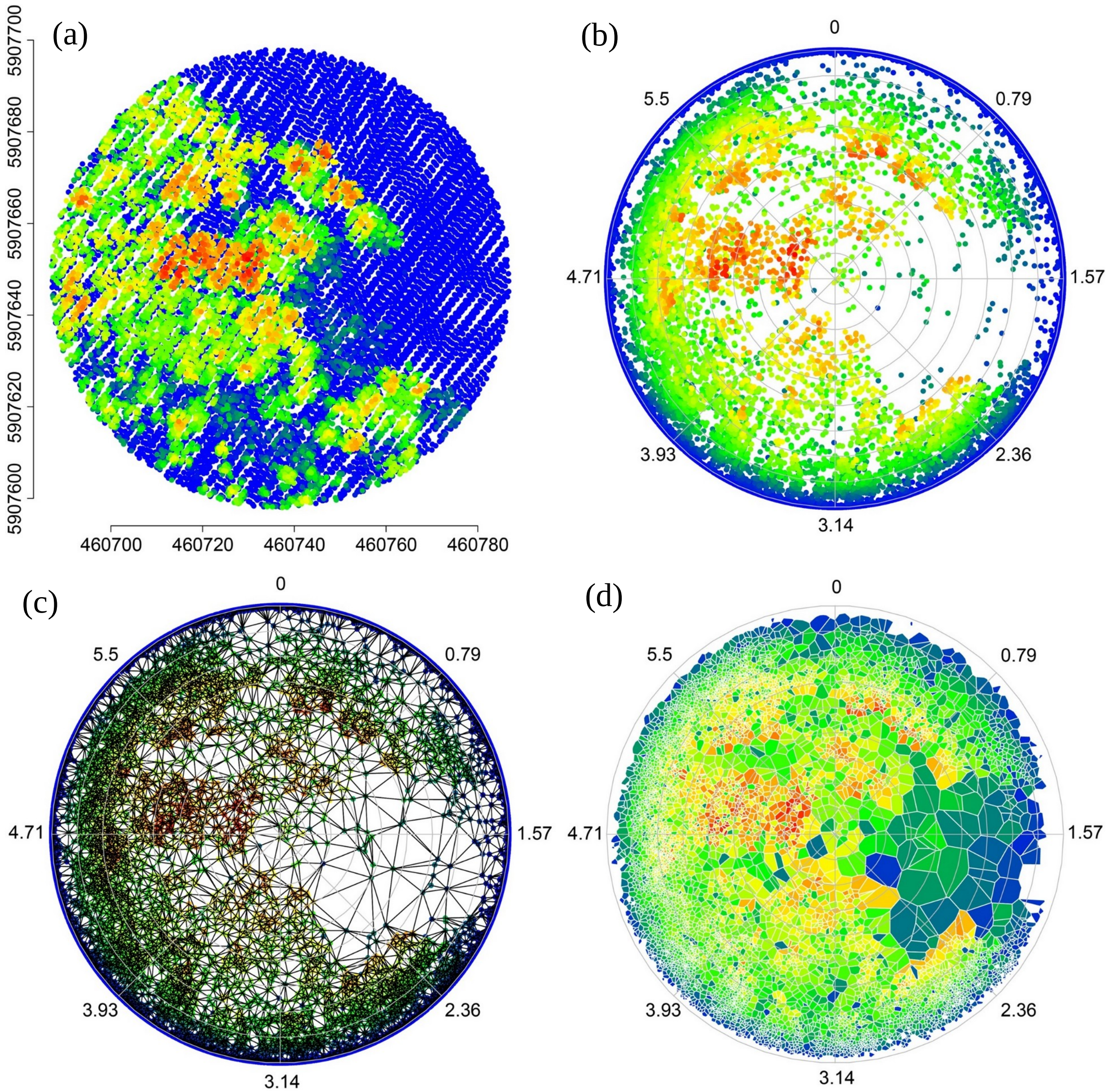

Figure 3. Example LiDAR plot process colored by point height (blue < green < red) with the orientation on-nadir and the circle units in radians with an equiangular projection: (a) nadir view of 50 m radius plot in NAD83 UTM 11N (meters) coordinates; (b) hemispherical view from the plot center toward the zenith projected in local coordinates; (c) Delaunay triangulation of hemispherically projected points; (d) Voronoi tessellation of hemispherically projected points

For the hemispherical view, multiple projections were tested, showing a significant impact on the estimation of ACC and P_o in the above results. The differences in projection are clearly visible for stereographic and orthographic projections, while subtle between equidistant and equiangular projections (Figure 4).

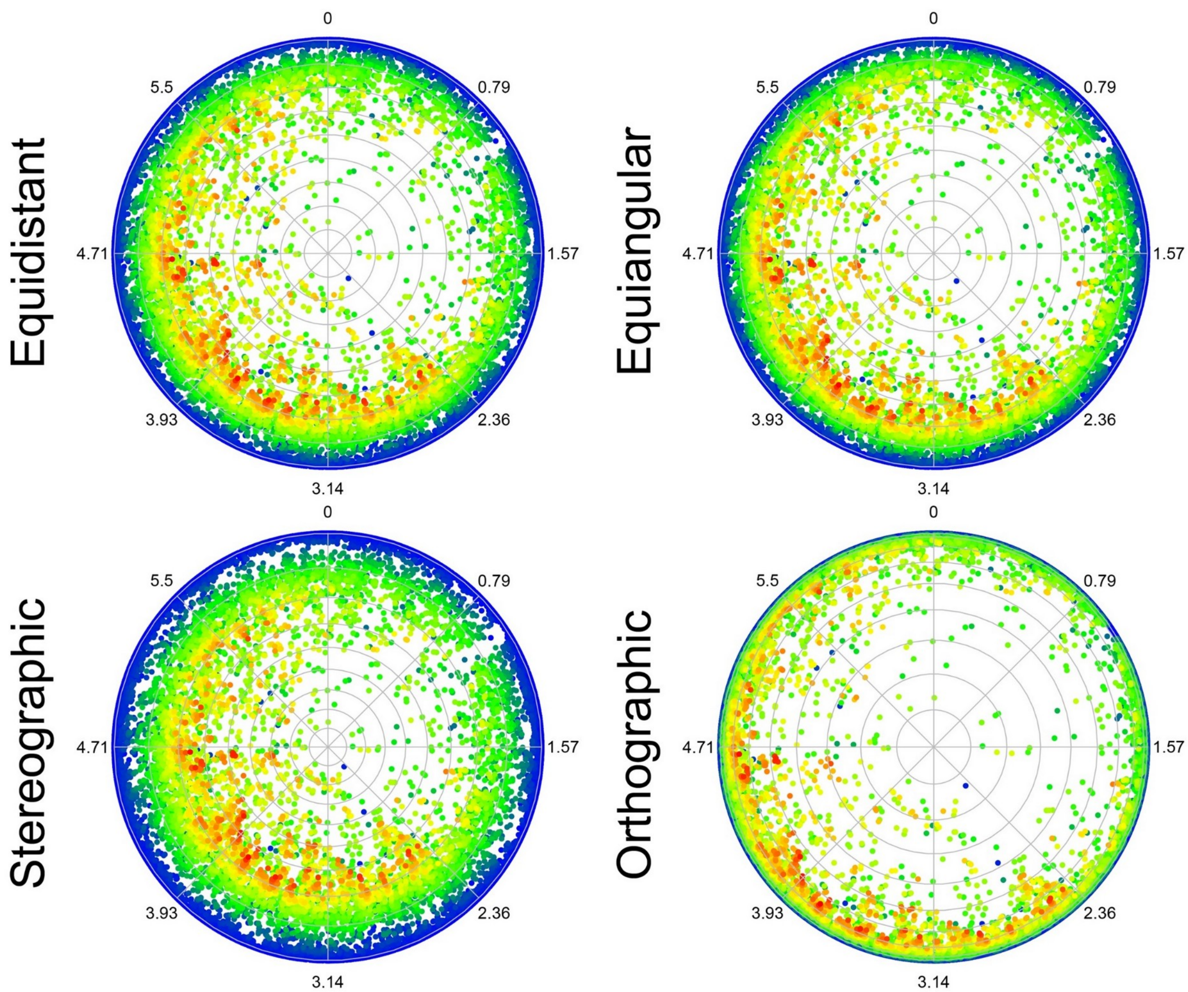

Figure 4. Example LiDAR plot demonstrating each of the four hemispherical (fisheye) lens geometries tested; colors represent point heights (blue < green < red); axis values are in radians

Applying the VCC_{fci} calculation to the full dataset of 950 ALS and ground plots, model fit improvement is again exhibited by filtering out disturbances. Both second-order polynomial (R^2 = 0.39) and exponential (R^2 = 0.35) models show reasonable model fit before filtering disturbed sites, followed by a simple linear model (R^2 = 0.32). After filtering out disturbed sites, model fit improved for the second-order polynomial model (R^2 = 0.43), exponential model (R^2 = 0.42), and linear model (R^2 = 0.40). Thus, linear and exponential models showed the greatest improvement in model fit, which is logical given their relatively inflexible behavior compared to polynomials.

Meanwhile, P_{pdn} showed strong linearity with ACC and thus P_o (Figure A2.5). Errors were higher at lower values of ACC, with the presence of a few strong outliers. The application of exponential and polynomial linear models were tested in terms of their impact on model performance (Table 3).

Table 3. Comparison of top three univariate ALS models (*VCC_{fci}*; *VCC_{fr}*; *VCC_{ir}*) with *P_{pdn}*; ACC = ground plot ACC; Exp(ACC) = exponential model ground ACC; Poly(ACC) 1 = first-order polynomial ground ACC; Poly(ACC) 2 = second-order polynomial ACC; Left model values = without filtering sites; Right model values = with filtering sites; standard error shown in parentheses

Dependent variable

	VCC_{fci}						VCC_{fr}					
Model	1	2	3	4	5	6	7	8	9	10	11	12
ACC	0.382*** (0.018)			0.757*** (0.035)			0.424*** (0.019)			0.770*** (0.036)		
Exp (ACC)		0.435*** (0.020)			0.435*** (0.020)			0.295*** (0.013)			0.440*** (0.020)	
Poly (ACC)1			-0.351*** (0.070)			-0.303 (0.186)			-0.230*** (0.076)			-0.078 (0.189)
Poly (ACC)2			0.989*** (0.092)			0.950*** (0.163)			0.884*** (0.099)			0.759*** (0.167)
b	0.280*** (0.010)	-0.317*** (0.038)	0.315*** (0.010)	0.031 (0.023)	-0.317*** (0.038)	0.301*** (0.052)	0.334*** (0.011)	0.041* (0.022)	0.364*** (0.011)	0.104*** (0.023)	-0.245*** (0.038)	0.320*** (0.053)
N	945	679	945	679	679	679	950	950	950	679	679	679
R^2	0.315	0.421	0.390	0.404	0.421	0.432	0.336	0.358	0.387	0.406	0.419	0.424
Adj.R^2	0.315	0.420	0.389	0.403	0.420	0.430	0.335	0.358	0.386	0.406	0.418	0.422
RSE	0.174 (df = 943)	0.135 (df = 677)	0.165 (df = 942)	0.137 (df = 677)	0.135 (df = 677)	0.134 (df = 676)	0.185 (df = 948)	0.182 (df = 948)	0.178 (df = 947)	0.138 (df = 677)	0.137 (df = 677)	0.137 (df = 676)
F-stat	434.237***(df = 1; 943)	492.101***(df = 1; 677)	301.499***(df = 2; 942)	457.978***(df = 1; 677)	492.101***(df = 1; 677)	256.980***(df = 2; 676)	478.719***(df = 1; 948)	529.045***(df = 1; 948)	298.685***(df = 2; 947)	463.670***(df = 1; 677)	488.157***(df = 1; 677)	248.980***(df = 2; 676)

	VCC_{ir}						P_{pdn}					
Model	13	14	15	16	17	18	19	20	21	22	23	24
ACC	0.265*** (0.014)			0.530*** (0.032)			-0.140*** (0.008)			-0.243*** (0.014)		
Exp (ACC)		0.310*** (0.018)			0.310*** (0.018)			-0.097*** (0.005)			-0.139*** (0.008)	-0.139*** (0.008)
Poly (ACC)1			-0.308*** (0.056)			-0.640*** (0.165)			0.061** (0.030)			
Poly (ACC)2			0.775*** (0.073)			1.049*** (0.146)			-0.272*** (0.040)			
b	0.178*** (0.008)	-0.252*** (0.034)	0.204*** (0.008)	0.002 (0.021)	-0.252*** (0.034)	0.300*** (0.046)	0.720*** (0.004)	0.816*** (0.009)	0.710*** (0.004)	0.788*** (0.009)	0.899*** (0.015)	0.899*** (0.015)
N	950	679	950	679	679	679	950	950	950	679	679	679
R^2	0.263	0.312	0.342	0.289	0.312	0.340	0.263	0.279	0.297	0.303	0.314	0.314
Adj.R^2	0.262	0.311	0.341	0.288	0.311	0.338	0.262	0.278	0.296	0.302	0.313	0.313
RSE	0.138 (df = 948)	0.122 (df = 677)	0.130 (df = 947)	0.124 (df = 677)	0.122 (df = 677)	0.119 (df = 676)	0.073 (df = 948)	0.072 (df = 948)	0.071 (df = 947)	0.055 (df = 677)	0.054 (df = 677)	0.054 (df = 677)
F-stat	338.476***(df = 1; 948)	307.218***(df = 1; 677)	246.053***(df = 2; 947)	275.828***(df = 1; 677)	307.218***(df = 1; 677)	174.242***(df = 2; 676)	337.608***(df = 1; 948)	366.773***(df = 1; 948)	200.322***(df = 2; 947)	294.661***(df = 1; 677)	309.682***(df = 1; 677)	309.682***(df = 1; 677)

*p<0.1; **p<0.05; ***p<0.01

Point-density normalized canopy gap fraction

The P_{pdn} algorithm produced reasonable results, showing agreement with other P_o estimates and measurements. A visualization of point-density-normalized gap fraction (P_{pdn}), Beer-Lambert Law gap fraction (P_{bl}), and Beer-Lambert Law effective leaf area index (Le_{bl}), and apparent clumping index (Ω_{app}) are provided for an example ALS field plot (Figure 5).

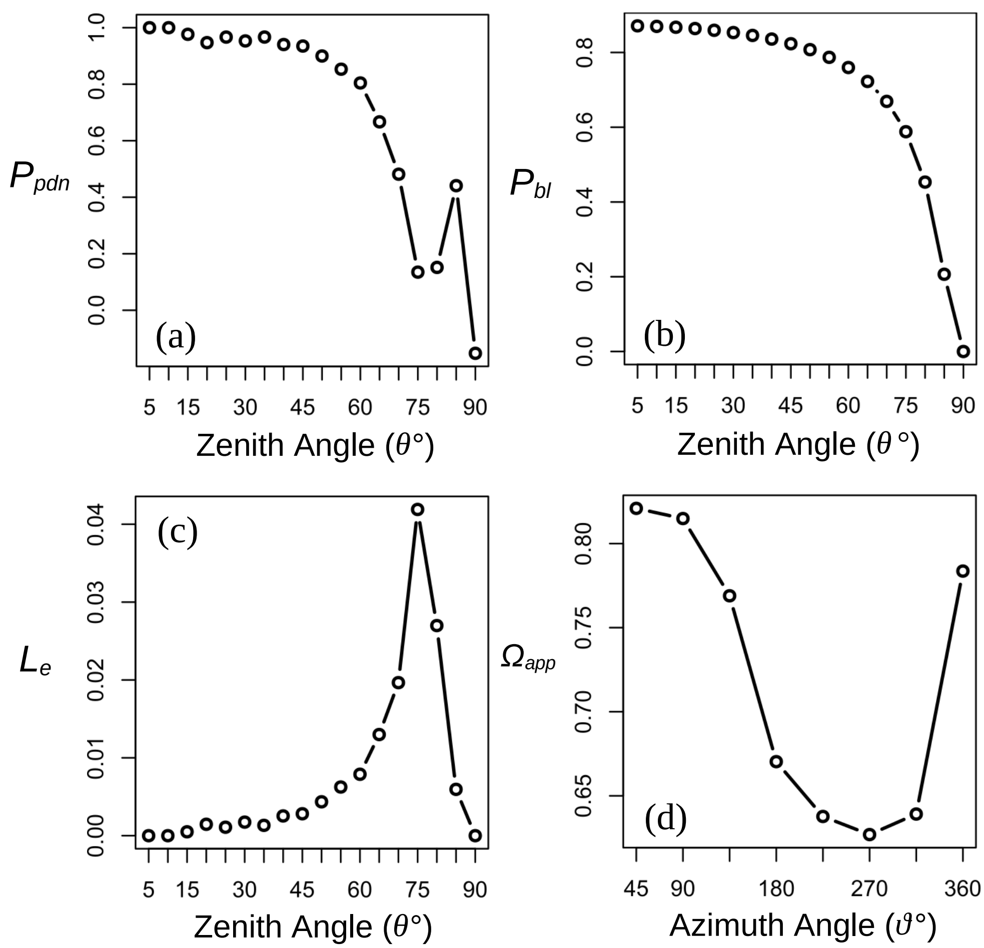

Figure 5. Comparison with traditional metrics: (a) point-density normalized gap fraction by zenith angle; (b) Beer-Lambert Law gap fraction by zenith angle; (c) Beer-Lambert Law effective leaf area index by zenith angle,

scaled by $\sin\theta$; (d) apparent clumping index by azimuth angle; y-axes represent respective values while x-axes represent zenith angle for (a), (b), and (c), and azimuth angle for (d)

Of the P_o metrics tested, the new P_{pdn} metric showed the best absolute correlation with ground measurements of ACC, topping other P_o metrics by a Pearson's r of nearly 0.2. A similar difference was shown for univariate linear model R^2 values, making P_{pdn} the top performing P_o metric tested. Nonetheless, the performance of P_o metrics may benefit from large improvements in accuracy by using deep learning models, such as PointNet++, which automatically learn features from data.For the height-to-crown area model used in ITC detection, first- and second-order polynomial models were chosen based on a visual analysis of plot data. Conifer species showed the best model fit, with a linear and polynomial R^2 of 0.94 and 0.98, respectively, compared to deciduous model R^2 values equal to 0.92 and 0.93. Both linear and second-order polynomial models for all species showed adequate performance ($R^2 = 0.88$; $R^2 = 0.89$). Hence, even though variation attributable to species is evident (Figure 6.7), a single polynomial linear model showing good model performance is used ($R^2 = 0.89$).

Variants of the ITC detection algorithms implemented here underwent validation in a number of previous studies (Kaartinen et al., 2012; Popescu et al., 2002). The algorithms were applied to generate predictor variables to test for variable importance in estimating canopy gap fraction (P_o), and its inverse, angular canopy closure (ACC). Herein, ITC results are treated as features for estimating T, rather than tree crown counts, as the purpose was to extract additional information from ALS data. Hence, the accuracy of their results is not a consideration in this work. From a visual analysis of ITC estimates, reasonable algorithm performance is assumed.

The ITC algorithms implemented include standard and hierarchical watershed segmentation, as well as standard and hierarchical variable-size moving window methods.

Standard and hierarchical variable-size moving window ITC detection counts of tree crowns performed the best in predicting ACC of the ITC methods, each with an R^2 above 0.4, despite not undergoing calibration. While ITC methods were not inferred to be able to predict ACC on their own, as ITC counts and ACC are considered dependent variables (Falkowski et al., 2008; Kaartinen et al., 2012; Wang et al., 2016), they are complimentary to other metrics as an additional feature of forest geometry, as is the apparent clumping index (Ω_{app}).

Discussion

While solar position, topography, and atmospheric conditions are known to effect the quantity and quality of understory light (Dengel et al., 2015), in this paper, we focus on canopy light transmission (T) indices best captured by LiDAR. This follows longstanding hemispherical photography research on canopy light transmission indices, including the gap light index or GLI/C (Canham, 1995, 1988) and the related Gap Light Analyzer or GLA (Frazer et al., 1999), as well as recent LiDAR methods aimed at characterizing broad areas at reduced time and cost (Korhonen and Morsdorf, 2014). Our proposed LiDAR canopy light transmission indices are intended for later application with statistical (e.g., machine learning) models to capture non-linear effects between canopy geometry, solar position, topography and atmospheric conditions on understory solar irradiation levels in large-area mapping efforts. This obviates the need for computationally expensive physical simulations at every grid cell.

Although previous studies show strong agreement with ground measurements for a number of ALS metrics of forest structure (Korhonen and Morsdorf, 2014), notable challenges remain. Models of canopy light transmission often utilize physically-based ray-tracing (Disney et al., 2000), which can be thought of as a synthetic LiDAR system, or are derived from simple canopy metrics such as Lorey's canopy height or leaf-area index (Niinemets and Anten, 2009). While the latter method lacks physical-geometric realism readily visible in existing point cloud datasets, the former also has its challenges. While radiative transfer models using ray-tracing may improve landscape-scale understory light estimates (Gastellu-Etchegorry et al., 2015; Moeser et al., 2014; Reich et al., 2012), ray-tracing requires high-point-density data (> 10 returns/m^2) from ALS or terrestrial laser scanning (TLS) LiDAR systems along with ancillary information beyond standard (*x*, *y*, *z*, *intensity*) information. Ray-tracing methods are also computationally demanding, making them slower and more expensive to apply. While deep reinforcement learning methods designed to accelerate ray-tracing algorithms through improved importance sampling may partially alleviate these challenges (Dahm and Keller, 2017), as demonstrated by Nvidia's latest RTX GPUs, ray-tracing remains computationally expensive.

In contrast, simple return-ratio approaches of quantifying canopy radiation attenuation may offer improved functioning with low-point-density data, simple, accelerated wall-to-wall mapping, and improved compatibility with historical ground-based methods needed to validate models with existing datasets or to analyze historical changes in forest strcuture. Furthermore, canopy attenuation-based ALS metrics may be comparable to methods used in the synthetic aperture RADAR community to estimate aboveground volume, such as the semi-empirical Water Cloud Model (Attema and Ulaby, 1978; Graham and Harris, 2003). Hence, ALS canopy radiation attenuation metrics may, in some limited capacity, be extensible to spaceborne RADAR sensors despite substantial differences in sensor design.

In this work, we presented and compared two new ALS indices of canopy light transmission to a suite of traditional metrics, demonstrated a new data filtering method to mitigate temporal lags providing substantial accuracy improvements, and performed perhaps the first analysis of data filtering and synthetic lens model effects on the calculation of LiDAR metrics. While none of the models tested showed excellent fit with ground ACC validation data, due to a mismatch between the date of ALS and ground data acquisition, one new gap fraction metric (P_{pdn}) showed a two-fold improvement over all other gap fraction methods tested. While the P_{hv} method did not perform as well, it nonetheless showed results comparable to traditional methods and a potential way forward for physical-geometric methods given its strong theoretical basis. The best performing models, after filtering out disturbed sites, saturated at R^2 values near 0.50. Our presented disturbed site filtering method often improved ALS metric R^2 values by over 0.1, or ~ 20%, without compromising the validity of the results. This contributes toward mitigating a long-standing challenge in remote sensing using a simple heuristic.

The overall top three metrics of ACC were all traditional VCC metrics: VCC_{fci}, VCC_{fr}, and VCC_{ir} all showed good univariate linear model fit with ground measurements (adjusted R^2 = 0.52; 0.51; 0.50). This work demonstrates that VCC and ACC metrics may be comparable in practice despite differences in conceptualization. This may be due to the angular nature of ALS acquisition, with relatively few samples occurring on-nadir. Such a hypothesis may be tested in future work by filtering data that varies off-nadir before calculating metrics. This study also showed that ITC detection methods provided one of the best proxies for ACC, which was unexpected and thus noteworthy.

Our new P_{hv} metric showed a low ACC R^2 saturation near 0.2 for all lens geometries even after filtering disturbed sites. Maximum R^2 values for the P_{hv} index were consistently shown for a canopy height threshold of 5 m. Of the lens geometries tested, the equisolid angle (equiangle) projection was shown to be the most sensitive to disturbances present in the observational record. Meanwhile, after filtering disturbed sites, differences in accuracy were more attributable to canopy height threshold than to lens model, with each lens model showing a similar R^2 pattern across tested threshold values. Meanwhile, the P_{pdn} metric may be considered a step toward the harmonization of ground-based and airborne estimates of P_o, which remains an outstanding challenge due to the different nature of ground and LiDAR measurement techniques. Finally, the excellent result for P_{pdn} and poor results for P_{hv} begs the question: *why do simple ratio-based models continue to outperform detailed geometric models?* We believe this is due to the sensitivity of highly detailed models to discrepancies in the validation data, which brings us to our study limitations.

Limitations

A fundamental limitation of this work was the half-decade difference in time between ground and ALS data acquisition, yielding strong disagreement between ground and ALS metrics of ACC for some sites. From ALS and field data scatterplots, it was apparent that disagreement arose either from disturbance or regrowth on previously disturbed sites. This temporal mismatch diminished the utility of ground ACC data for use in model validation, as shown by model performance after filtering disturbed sites. This gave rise to a second question present throughout the duration of this study: *why do we still use spherical densiometers for remote sensing model validation in 2019?* Although the ALS data had a low mean point density of 1.64 points/m^2, these active data are of greater geolocation accuracy, precision, and sampling density than passive coarse spherical densiometer measurements. Presently, it would not be unreasonable to treat LiDAR itself as ground-truth data, given its superior characteristics by most metrics.

Thus, we question the use of coarse ground measurements of ACC (e.g., spherical densiometers), instead arguing for modern LiDAR systems, structure-from-motion (SfM), real-time simultaneous localization and mapping (SLAM), 360-degree spherical imagers (e.g., FLIR Ladybug), or digital hemispherical imagers. Today, the average smartphone imager provides greater information about canopy geometry than spherical densiometers, including an ability to produce 3-D SfM or SLAM point clouds and to display the produced 3-D models using built-in augmented reality (AR) interfaces running on onboard graphics accelerators (e.g., ARM Mali, Apple A12 Bionic, Qualcomm Adreno 640). The use of full-waveform data may further add state-of-the-art vertical canopy sampling and canopy penetration essential for modeling canopy light transmission. Yet, historical spherical densiometer data was essential for the completion of this study and methods will continue to be in demand that are able to cope with densiometer data for global change studies. For such applications, we provide the new P_{pdn} metric and for detailed geometric datasets, we provide the new P_{hv} metric.

As a result of the aforementioned data limitations, none of the P_{hv} methods tested show strong performance, requiring further validation against hemispherical photography measurements closer to the time of ALS acquisition. This is indicated by the strong agreement between multiple LiDAR-derived predictors of ACC showing only moderate agreement with convex spherical densiometer measurements. While step-wise AIC and BIC linear regression models included high numbers of coefficients without substantial performance gains, univariate linear models showed equivalent performance. We infer that this temporal mismatch poses a fundamental limitation on algorithm performance in this study, as top-performing metrics saturate near the same accuracy level.

Conclusion

This work demonstrated two important new algorithms for modeling of forest structure applicable to multiple types of point cloud data (e.g., ALS, TLS, SfM), as well as a method for filtering disturbed sites. While our study was limited by the quality and acquisition timing of field data, we found that the P_{pdn} metric in particular showed strong performance. In addition, we showed that filtering sites and canopy threshold height have a greater effect on P_{hv} performance than the synthetic lens model. Meanwhile, traditional VCC metrics still showed the best overall corrrespondances to ACC measurements, despite being fundamentally different in principle.

From these results, we concluded that the new ALS-based models of T are promising, yet require further development with higher point densities closer to the time of ground data acquisition. Those with high point density LiDAR datasets may nonetheless benefit from the methods presented above, necessary for pursuing similar studies in regions where there is limited ground sampling coverage, as is often the case in boreal forests. These new metrics in turn are likely to be overcome by unsupervised feature learning (i.e., deep learning) applied to high-point-density datasets.

As point densities increase with technological advances, and spectral data are embedded to points (e.g., SfM or multi-spectral ALS systems), traditional ground measurement techniques may be less relevant for model validation. We argue that point cloud models are sufficient in their own right for the estimation of canopy geometric properties, such as coverage or closure. Future studies should move beyond historical ground measurement techniques of canopy light transmission to explore the use of synthetic data under idealized conditions. By generating idealized point clouds of forests (evenly spaced 1 point/mm^2) using a latest generation 3-D simulation framework, and iterating over random samples from these, robust physical features may be engineered that function across a variety of forest conditions. Such physically-based rendering tools are also ideal for the generation of large labeled datasets needed to train state-of-the-art supervised learning models, overcoming the central factor limiting the application of deep learning in LiDAR remote sensing of forests.

Acknowledgements

A.E. proposed and conducted this research and authored the original manuscript, as well as subsequent versions. N.C. provided manuscript edits and generously supported this research in his laboratory. Field inventory data for this study was generously provided by Scott Nielsen of University of Alberta. This work was generously funded by Foothills Research Association’s Grizzly Bear Program and an NSERC grant to N.C.

References

Aakala, T., Shimatani, K., Abe, T., Kubota, Y., Kuuluvainen, T., 2016. Crown asymmetry in high latitude forests: disentangling the directional effects of tree competition and solar radiation. Oikos 125, 1035–1043. https://doi.org/10.1111/oik.02858

Abraham, S., Förstner, W., 2005. Fish-eye-stereo calibration and epipolar rectification. ISPRS J. Photogramm. Remote Sens. 59, 278–288. https://doi.org/http://dx.doi.org/10.1016/j.isprsjprs.2005.03.001

Alexander, C., Moeslund, J.E., Bøcher, P.K., Arge, L., Svenning, J.-C., 2013. Airborne laser scanner (LiDAR) proxies for understory light conditions. Remote Sens. Environ. 134, 152–161. https://doi.org/http://dx.doi.org/10.1016/j.rse.2013.02.028

Attema, E.P.W., Ulaby, F.T., 1978. Vegetation modeled as a water cloud. Radio Sci. 13, 357–364. https://doi.org/10.1029/RS013i002p00357

Axelsson, P., 1999. Processing of laser scanner data—algorithms and applications. ISPRS J. Photogramm. Remote Sens. 54, 138–147. https://doi.org/http://dx.doi.org/10.1016/S0924-2716(99)00008-8

Barnes, C., Tibbitts, T., Sager, J., Deitzer, G., Bubenheim, D., Koerner, G., Bugbee, B., 1993. Accuracy of quantum sensors measuring yield photon flux and photosynthetic photon flux. HortScience 28, 1197–1200.

Canham, C., 1995. GLI/C: Software for calculation of light transmission through forest canopies using colour fisheye photography. Millbrook, NY, USA.

Canham, C.D., 1988. An Index For Understory Light Levels in and Around Canopy Gaps. Ecology 69, 1634–1638. https://doi.org/10.2307/1941664

Canham, C.D., Coates, K.D., Bartemucci, P., Quaglia, S., 1999. Measurement and modeling of spatially explicit variation in light transmission through interior cedar-hemlock forests of British Columbia. Can. J. For. Res. 29, 1775–1783. https://doi.org/10.1139/x99-151

Coops, N., Hilker, T., Wulder, M., St-Onge, B., Newnham, G., Siggins, A., Trofymow, J.A. (Tony), 2007. Estimating canopy structure of Douglas-fir forest stands from discrete-return LiDAR. Trees 21, 295–310. https://doi.org/10.1007/s00468-006-0119-6

Cortini, F., Filipescu, C.N., Groot, A., MacIsaac, D.A., Nunifu, T., 2011. Regional models of diameter as a function of individual tree attributes, climate and site characteristics for six major tree species in Alberta, Canada. Forests 2, 814. https://doi.org/10.3390/f2040814

Coyle, D.B., Stysley, P.R., Poulios, D., Clarke, G.B., Kay, R.B., 2015. Laser transmitter development for NASA's Global Ecosystem Dynamics Investigation (GEDI) lidar, in: Proc. SPIE 9612, Lidar Remote Sensing for Environmental Monitoring XV, 961208 (September 1, 2015). SPIE, San Diego, CA, USA, pp. 961207–961208.

Dahm, K., Keller, A., 2017. Learning Light Transport the Reinforced Way, in: ACM SIGGRAPH 2017. ACM, Los Angeles, CA, USA, pp. 73:1-73:2. https://doi.org/10.1145/3084363.3085032

Dengel, S., Grace, J., 2010. Carbon dioxide exchange and canopy conductance of two coniferous forests under various sky conditions. Oecologia 164, 797–808. https://doi.org/10.1007/s00442-010-1687-0

Dengel, S., Grace, J., MacArthur, A., 2015. Transmissivity of solar radiation within a Picea sitchensis stand under various sky conditions. Biogeosciences 12, 4195–4207. https://doi.org/10.5194/bg-12-4195-2015

Disney, M.I., Lewis, P., North, P.R.J., 2000. Monte Carlo ray tracing in optical canopy reflectance modelling. Remote Sens. Rev. 18, 163–196. https://doi.org/10.1080/02757250009532389

Domingos, P., 2012. A few useful things to know about machine learning. Commun. ACM 55, 78–87. https://doi.org/10.1145/2347736.2347755

Dubayah, R., Goetz, S.J., Blair, J.B., Fatoyinbo, T.E., Hansen, M., Healey, S.P., Hofton, M.A., Hurtt, G.C., Kellner, J., Luthcke, S.B., Swatantran, A., 2014. The Global Ecosystem Dynamics Investigation, in: AGU Fall Meeting 2014.

Eysn, L., Hollaus, M., Lindberg, E., Berger, F., Monnet, J.-M., Dalponte, M., Kobal, M., Pellegrini, M., Lingua, E., Mongus, D., Pfeifer, N., 2015. A benchmark of Lidar-based single tree detection methods using heterogeneous forest data from the alpine space. Forests 6, 1721. https://doi.org/10.3390/f6051721

Falkowski, M.J., Smith, A.M.S., Gessler, P.E., Hudak, A.T., Vierling, L.A., Evans, J.S., 2008. The influence of conifer forest canopy cover on the accuracy of two individual tree measurement algorithms using lidar data. Can. J. Remote Sens. 34, S338–S350. https://doi.org/10.5589/m08-055

Frazer, G.W., Canham, C.D., Lertzman, K.P., 1999. Gap Light Analyzer (GLA), Version 2.0: Imaging software to extract canopy structure and gap light transmission indices from true-colour fisheye photographs, user manual and program documentation. Burnaby, BC, Canada; Millbrook, NY, USA.

Gamon, J.A., 2014. Can vegetation optical types help address plant-climate interactions?, in: AGU Fall Meeting. American Geophysical Union, San Francisco, CA.

Gamon, J.A., Bond, B., 2013. Effects of irradiance and photosynthetic downregulation on the photochemical reflectance index in Douglas-fir and ponderosa pine. Remote Sens. Environ. 135, 141–149. https://doi.org/http://dx.doi.org/10.1016/j.rse.2013.03.032

Gastellu-Etchegorry, J.-P., Yin, T., Lauret, N., Cajgfinger, T., Gregoire, T., Grau, E., Feret, J.-B., Lopes, M., Guilleux, J., Dedieu, G., Malenovský, Z., Cook, B.D., Morton, D., Rubio, J., Durrieu, S., Cazanave, G., Martin, E., Ristorcelli, T., 2015. Discrete anisotropic radiative transfer (DART 5) for modeling airborne and satellite spectroradiometer and LIDAR acquisitions of natural and urban landscapes. Remote Sens. 7, 1667. https://doi.org/10.3390/rs70201667

Gastellu-Etchegorry, J.P., Demarez, V., Pinel, V., Zagolski, F., 1996. Modeling radiative transfer in heterogeneous 3-D vegetation canopies. Remote Sens. Environ. 58, 131–156. https://doi.org/http://dx.doi.org/10.1016/0034-4257(95)00253-7

Gonsamo, A., D'odorico, P., Pellikka, P., 2013. Measuring fractional forest canopy element cover and openness – definitions and methodologies revisited. Oikos 122, 1283–1291. https://doi.org/10.1111/j.1600-0706.2013.00369.x

Graham, A.J., Harris, R., 2003. Extracting biophysical parameters from remotely sensed radar data: a review of the water cloud model. Prog. Phys. Geogr. 27, 217–229.

Hancock, S., 2010. Understanding the measurement of forests with waveform lidar. University College London.

Hilker, T., Coops, N.C., Newnham, G.J., van Leeuwen, M., Wulder, M.A., Stewart, J., Culvenor, D.S., 2012. Comparison of terrestrial and airborne LiDAR in describing stand structure of a thinned lodgepole pine forest. J. For. 110, 97-104(8).

Hilker, T., Frazer, G.W., Coops, N.C., Wulder, M.A., Newnham, G.J., Stewart, J.D., van Leeuwen, M., Culvenor, D.S., 2013. Prediction of wood fiber attributes from LiDAR-derived forest canopy indicators. For. Sci. 59, 231–242. https://doi.org/doi:10.5849/forsci.11-074

Hopkinson, C., Chasmer, L., 2009. Testing LiDAR models of fractional cover across multiple forest ecozones. Remote Sens. Environ. 113, 275–288. https://doi.org/http://dx.doi.org/10.1016/j.rse.2008.09.012

Hopkinson, C., Chasmer, L., 2007. Modelling canopy gap fraction from lidar intensity, in: ISPRS Laser Scanning 2007 and SilviLaser 2007. Espoo, Finland, pp. 190–194.

Isenburg, M., 2015. LAStools: Efficient LiDAR processing software.

Isenburg, M., Liu, Y., Shewchuk, J., Snoeyink, J., 2006a. Streaming computation of Delaunay triangulations, in: Proceedings of SIGGRAPH. Boston, USA, pp. 1049–1056.

Isenburg, M., Liu, Y., Shewchuk, J., Snoeyink, J., Thirion, T., 2006b. Generating raster DEM from mass points via TIN streaming, in: Raubal, M., Miller, H.J., Frank, A.U., Goodchild, M.F. (Eds.), Geographic Information Science, 4th International Conference, GIScience 2006, Lecture Notes in Computer Science. Springer, Münster, Germany, pp. 186–198. https://doi.org/10.1007/11863939

Isenburg, M., Liu, Y., Snoeyink, J., 2006c. Streaming extraction of elevation contours from LIDAR points. Chapel Hill, NC, USA.

Kaartinen, H., Hyyppä, J., Yu, X., Vastaranta, M., Hyyppä, H., Kukko, A., Holopainen, M., Heipke, C., Hirschmugl, M., Morsdorf, F., Næsset, E., Pitkänen, J., Popescu, S., Solberg, S., Wolf, B.M., Wu, J.-C., 2012. An international comparison of individual tree detection and extraction using airborne laser scanning. Remote Sens. 4, 950. https://doi.org/10.3390/rs4040950

Khosravipour, A., Skidmore, A.K., Isenburg, M., 2016. Generating spike-free digital surface models using LiDAR raw point clouds: A new approach for forestry applications. Int. J. Appl. Earth Obs. Geoinf. 52, 104–114. https://doi.org/http://dx.doi.org/10.1016/j.jag.2016.06.005

Khosravipour, A., Skidmore, A.K., Isenburg, M., Wang, T., Hussin, Y.A., 2014. Generating pit-free canopy height models from airborne Lidar. Photogramm. Eng. Remote Sens. 80, 863–872. https://doi.org/10.14358/PERS.80.9.863

Korhonen, L., Korpela, I., Heiskanen, J., Maltamo, M., 2011. Airborne discrete-return LIDAR data in the estimation of vertical canopy cover, angular canopy closure and leaf area index. Remote Sens. Environ. 115, 1065–1080. https://doi.org/http://dx.doi.org/10.1016/j.rse.2010.12.011

Korhonen, L., Morsdorf, F., 2014. Estimation of canopy cover, gap fraction and leaf area index with airborne laser scanning, in: Maltamo, M., Næsset, E., Vauhkonen, J. (Eds.), Forestry Applications of Airborne Laser Scanning: Concepts and Case Studies. Springer Netherlands, Dordrecht, pp. 397–417. https://doi.org/10.1007/978-94-017-8663-8_20

Kraus, K., Pfeifer, N., 1998. Determination of terrain models in wooded areas with airborne laser scanner data. ISPRS J. Photogramm. Remote Sens. 53, 193–203. https://doi.org/http://dx.doi.org/10.1016/S0924-2716(98)00009-4

Lang, A.R.G., Yueqin, X., 1986. Estimation of leaf area index from transmission of direct sunlight in discontinuous canopies. Agric. For. Meteorol. 37, 229–243.

https://doi.org/http://dx.doi.org/10.1016/0168-1923(86)90033-X

Lee, H., Slatton, K.C., Roth, B.E., Cropper, W.P., 2008. Prediction of forest canopy light interception using three-dimensional airborne LiDAR data. Int. J. Remote Sens. 30, 189–207. https://doi.org/10.1080/01431160802261171

Lefsky, M.A., Cohen, W.B., Parker, G.G., Harding, D.J., 2002. Lidar remote sensing for ecosystem studies. Bioscience 52, 19–30. https://doi.org/10.1641/0006-3568(2002)052[0019:LRSFES]2.0.CO;2

Lemon, P.E., 1956. A spherical densiometer for estimating forest overstory density. For. Sci. 2, 314–320.

Maguya, A.S., Junttila, V., Kauranne, T., 2014. Algorithm for extracting digital terrain models under forest canopy from airborne LiDAR data. Remote Sens. 6, 6524–6548. https://doi.org/10.3390/rs6076524

Miller, J.B., 1967. A formula for average foliage density. Aust. J. Bot. 15, 141–144.

Moeser, D., Morsdorf, F., Jonas, T., 2015. Novel forest structure metrics from airborne LiDAR data for improved snow interception estimation. Agric. For. Meteorol. 208, 40–49. https://doi.org/http://dx.doi.org/10.1016/j.agrformet.2015.04.013

Moeser, D., Roubinek, J., Schleppi, P., Morsdorf, F., Jonas, T., 2014. Canopy closure, LAI and radiation transfer from airborne LiDAR synthetic images. Agric. For. Meteorol. 197, 158–168. https://doi.org/http://dx.doi.org/10.1016/j.agrformet.2014.06.008

Monsi, M., Saeki, T., 2005. On the factor light in plant communities and its importance for matter production. Ann. Bot. 95, 549–567. https://doi.org/10.1093/aob/mci052

Monsi, M., Saeki, T., 1953. Über den Lichtfaktor in den Pflanzengesellschaften und seine

Bedeutung für die Stoffproduktion. Japanese J. Bot. 14, 22–52.

Morsdorf, F., Kötz, B., Meier, E., Itten, K.I., Allgöwer, B., 2006. Estimation of LAI and fractional cover from small footprint airborne laser scanning data based on gap fraction. Remote Sens. Environ. 104, 50–61. https://doi.org/http://dx.doi.org/10.1016/j.rse.2006.04.019

Musselman, K.N., Margulis, S.A., Molotch, N.P., 2013. Estimation of solar direct beam transmittance of conifer canopies from airborne LiDAR. Remote Sens. Environ. 136, 402–415. https://doi.org/http://dx.doi.org/10.1016/j.rse.2013.05.021

Natural Regions Committee, 2006. Natural Regions and Subregions of Alberta. Government of Alberta, Edmonton, AB, Canada.

Nielsen, S.E., 2005. Habitat ecology, conservation, and projected population viability of grizzly bears (Ursus Arctos L.) in west-central Alberta, Canada. University of Alberta, Edmonton, AB, Canada.

Nielsen, S.E., Munro, R.H.M., Bainbridge, E.L., Stenhouse, G.B., Boyce, M.S., 2004. Grizzly bears and forestry. For. Ecol. Manage. 199, 67–82. https://doi.org/10.1016/j.foreco.2004.04.014

Nielsen, S.E., Stenhouse, G.B., Boyce, M.S., 2006. A habitat-based framework for grizzly bear conservation in Alberta. Biol. Conserv. 130, 217–229. https://doi.org/10.1016/j.biocon.2005.12.016

Niinemets, Ü., Anten, N.P.R., 2009. Packing the photosynthetic machinery: From leaf to canopy, in: Laisk, A., Nedbal, L., Govindjee (Eds.), Photosynthesis in Silico: Understanding Complexity from Molecules to Ecosystems. Springer Netherlands, Dordrecht, pp. 363–399.

https://doi.org/10.1007/978-1-4020-9237-4_16

Parent, J.R., Volin, J.C., 2014. Assessing the potential for leaf-off LiDAR data to model canopy closure in temperate deciduous forests. ISPRS J. Photogramm. Remote Sens. 95, 134–145. https://doi.org/http://dx.doi.org/10.1016/j.isprsjprs.2014.06.009

Parker, G.G., Lefsky, M.A., Harding, D.J., 2001. Light transmittance in forest canopies determined using airborne laser altimetry and in-canopy quantum measurements. Remote Sens. Environ. 76, 298–309. https://doi.org/http://dx.doi.org/10.1016/S0034-4257(00)00211-X

Popescu, S.C., Wynne, R.H., Nelson, R.F., 2002. Estimating plot-level tree heights with lidar: local filtering with a canopy-height based variable window size. Comput. Electron. Agric. 37, 71–95. https://doi.org/http://dx.doi.org/10.1016/S0168-1699(02)00121-7

Popescu, S.C., Wynne, R.H., Scrivani, J.A., 2004. Fusion of small-footprint lidar and multispectral data to estimate plot-level volume and biomass in deciduous and pine forests in Virginia, USA. For. Sci. 50, 551–565.

Qi, C.R., Yi, L., Su, H., Guibas, L.J., 2017. PointNet++: Deep Hierarchical Feature Learning on Point Sets in a Metric Space. arXiv e-prints arXiv:1706.02413.

R Core Team, 2015. R: A Language and Environment for Statistical Computing.

Ray, S.F., 2002. Applied Photographic Optics, 3rd ed. Focal Press.

Reich, P.B., Frelich, L.E., Voldseth, R.A., Bakken, P., Adair, E.C., 2012. Understorey diversity in southern boreal forests is regulated by productivity and its indirect impacts on resource availability and heterogeneity. J. Ecol. 100, 539–545. https://doi.org/10.1111/j.1365-2745.2011.01922.x

Riaño, D., Valladares, F., Condés, S., Chuvieco, E., 2004. Estimation of leaf area index and covered ground from airborne laser scanner (Lidar) in two contrasting forests. Agric. For. Meteorol. 124, 269–275. https://doi.org/http://dx.doi.org/10.1016/j.agrformet.2004.02.005

Richardson, J.J., Moskal, L.M., Kim, S.-H., 2009. Modeling approaches to estimate effective leaf area index from aerial discrete-return LIDAR. Agric. For. Meteorol. 149, 1152–1160. https://doi.org/http://dx.doi.org/10.1016/j.agrformet.2009.02.007

Ryu, Y., Nilson, T., Kobayashi, H., Sonnentag, O., Law, B.E., Baldocchi, D.D., 2010. On the correct estimation of effective leaf area index: Does it reveal information on clumping effects? Agric. For. Meteorol. 150, 463–472. https://doi.org/http://dx.doi.org/10.1016/j.agrformet.2010.01.009

Shean, D.E., Alexandrov, O., Moratto, Z.M., Smith, B.E., Joughin, I.R., Porter, C., Morin, P., 2016. An automated, open-source pipeline for mass production of digital elevation models (DEMs) from very-high-resolution commercial stereo satellite imagery. ISPRS J. Photogramm. Remote Sens. 116, 101–117. https://doi.org/http://dx.doi.org/10.1016/j.isprsjprs.2016.03.012

Shepard, D., 1968. A two-dimensional interpolation function for irregularly-spaced data, in: Proceedings of the 1968 23rd ACM National Conference, ACM 1968. Association for Computing Machinery, New York, NY, USA, pp. 517–524. https://doi.org/10.1145/800186.810616

Solberg, S., Brunner, A., Hanssen, K.H., Lange, H., Næsset, E., Rautiainen, M., Stenberg, P., 2009. Mapping LAI in a Norway spruce forest using airborne laser scanning. Remote Sens. Environ. 113, 2317–2327. https://doi.org/http://dx.doi.org/10.1016/j.rse.2009.06.010

Turner, R., 2015. deldir: Delaunay triangulation and Dirichlet (Voronoi) tessellation.

Vaccari, S., van Leeuwen, M., Calders, K., Coops, N.C., Herold, M., 2013. Bias in lidar-based canopy gap fraction estimates. Remote Sens. Lett. 4, 391–399. https://doi.org/10.1080/2150704X.2012.742211

Varhola, A., Frazer, G.W., Teti, P., Coops, N.C., 2012. Estimation of forest structure metrics relevant to hydrologic modelling using coordinate transformation of airborne laser scanning data. Hydrol. Earth Syst. Sci. 16, 3749–3766. https://doi.org/10.5194/hess-16-3749-2012

Wang, Y., Hyyppä, J., Liang, X., Kaartinen, H., Yu, X., Lindberg, E., Holmgren, J., Qin, Y., Mallet, C., Ferraz, A., Torabzadeh, H., Morsdorf, F., Zhu, L., Liu, J., Alho, P., 2016. International benchmarking of the individual tree detection methods for modeling 3-D canopy structure for silviculture and forest ecology using airborne laser scanning. IEEE Trans. Geosci. Remote Sens. https://doi.org/10.1109/TGRS.2016.2543225

Warren, J., Schaefer, S., Hirani, A.N., Desbrun, M., 2006. Barycentric coordinates for convex sets. Adv. Comput. Math. 27, 319–338. https://doi.org/10.1007/s10444-005-9008-6

Weiss, M., Baret, F., Smith, G.J., Jonckheere, I., Coppin, P., 2004. Review of methods for in situ leaf area index (LAI) determination: Part II. Estimation of LAI, errors and sampling. Agric. For. Meteorol. 121, 37–53. https://doi.org/http://dx.doi.org/10.1016/j.agrformet.2003.08.001

Wulder, M.A., White, J.C., Nelson, R.F., Næsset, E., Ørka, H.O., Coops, N.C., Hilker, T., Bater, C.W., Gobakken, T., 2012. Lidar sampling for large-area forest characterization: A review. Remote Sens. Environ. 121, 196–209. https://doi.org/http://dx.doi.org/10.1016/j.rse.2012.02.001

Zhao, K., Popescu, S., 2009. Lidar-based mapping of leaf area index and its use for validating

GLOBCARBON satellite LAI product in a temperate forest of the southern USA. Remote Sens. Environ. 113, 1628–1645. https://doi.org/http://dx.doi.org/10.1016/j.rse.2009.03.006

Zimble, D.A., Evans, D.L., Carlson, G.C., Parker, R.C., Grado, S.C., Gerard, P.D., 2003. Characterizing vertical forest structure using small-footprint airborne LiDAR. Remote Sens. Environ. 87, 171–182. https://doi.org/http://dx.doi.org/10.1016/S0034-4257(03)00139-1